



1 **Turbulent erosion of a subducting intrusion in the Western** 2 **Mediterranean Sea**

3 Giovanni Testa¹, Mathieu Dever^{2,3}, Mara Freilich⁴, Amala Mahadevan², T. M. Shaun Johnston⁵, Lorenzo
4 Pasculli^{1,6}, Francesco M. Falcieri¹

5 ¹ Institute of Marine Sciences, Italian National Research Council (CNR-ISMAR), Venice, Italy.

6 ² Woods Hole Oceanographic Institution, Woods Hole, 02543, MA, USA

7 ³ RBR, Ottawa, Canada

8 ⁴ Brown University, Providence, RI, USA

9 ⁵ Scripps Institution of Oceanography, University of California, San Diego, La Jolla, CA, USA

10 ⁶ Department of Environmental Sciences, Informatics and Statistics, University Ca' Foscari of Venice, Via Torino 155, 30172
11 Mestre, Italy

12 *Correspondence to:* Giovanni Testa (giovanni.testa@ve.ismar.cnr.it)

13 **Abstract.** Frontal zones within the Western Alboran Gyre (WAG) are characterized by a density gradient resulting from the
14 convergence of Atlantic and Mediterranean waters. Subduction along isopycnals at the WAG periphery can play a crucial role
15 in upper ocean ventilation and influences its stratification and biogeochemical cycles. In 2019, physical parameters
16 (comprising temperature, salinity, turbulent kinetic energy dissipation rates) and biogeochemical data (oxygen and
17 chlorophyll-a) profiles were collected in transects along the northern edge of the WAG. Several intrusions of subducted water
18 with elevated oxygen, chlorophyll-a and spice anomaly were identified towards the center of the anticyclone. These features
19 had elevated kinetic energy dissipation rates on both their upper and lower boundaries. Analysis of the turbulent fluxes
20 involving heat, salt, oxygen, and chlorophyll-a demonstrated a net flux of physical and biogeochemical properties from the
21 intrusions to the surrounding ocean. Either the turbulent or diffusive convection mixing contributed to the observed dilution
22 of the intrusion. Other factors (e.g., water column density stability, variability of the photic layer depth, and organic matter
23 degradation) likely played a role in these dynamics. Enhanced comprehension of the persistence and extent of these features
24 might lead to an improved quantitative parametrization of relevant physical and biogeochemical properties involved in
25 subduction within the study zone.

26 **1 Introduction**

27 The Mediterranean Sea is characterized by a shallow circulation cell and a complex upper-layer circulation featuring numerous
28 quasi-permanent eddies and fronts (Tanhua et al., 2013; Capó et al., 2019; Barral et al., 2021; Bonaduce et al., 2021;
29 Zarokanellos et al., 2022; Sánchez-Garrido and Nadal, 2022). The main 12 Mediterranean thermal fronts were listed by Belkin
30 and Cornillon (2007), whereas a recent work by Sudre et al. (2023) captured an even more complex scenario. Specifically,
31 frontal zones in the Alboran Sea (Western Mediterranean basin) are characterized by a density gradient resulting from the



32 convergence of Atlantic and Mediterranean waters (Fedele et al., 2022; Garcia-Jove et al., 2022). The Atlantic jet strongly
33 influences the formation of two large-scale anticyclonic gyres within the Alboran Sea (the Eastern and Western Alboran Gyres,
34 WAG; **Fig. 1A**) with a smaller cyclonic gyre typically situated in between (Brett et al., 2020; Sala et al., 2022; Sánchez-Garrido
35 and Nadal, 2022).

36 Ocean subduction, defined as the physical transfer of water from the mixed layer into the ocean interior (Williams,
37 2001), plays a pivotal role in upper-ocean ventilation and stratification. It also exerts a profound influence on biogeochemical
38 cycles, thereby contributing to the export of greenhouse gases and the vertical transport of organic carbon (Omand et al., 2015;
39 Olita et al., 2017; Stukel et al., 2017; Ruiz et al., 2019; Zarokanellos et al., 2022). The vertical component of ocean current
40 velocity is typically much smaller than its horizontal counterparts, but areas characterized by meandering frontal features
41 associated with mesoscale eddies are expected to exhibit elevated subduction rates (van Haren et al., 2006). Indeed, vertical
42 velocities of up to 55 m d^{-1} have been observed in the Western Alboran Sea front (Capó and McWilliams, 2022; Garcia-Jove
43 et al., 2022; Rudnick et al., 2022), and net submesoscale subduction rate has been estimated at 0.3 m day^{-1} (Freilich and
44 Mahadevan, 2021). Mesoscale turbulence contains more energy than submesoscale patterns (Storer et al., 2022), although
45 submesoscale features can generate larger vertical velocities than mesoscale structures within frontal zones (Mahadevan, 2016;
46 Ruiz et al., 2019). The relationship between submesoscale velocity and turbulence within the boundary layer has been explored
47 in prior studies under conditions of turbulent thermal wind balance (Crowe and Taylor, 2018; McWilliams, 2021) and
48 symmetric instabilities (Thomas et al., 2013; Bachman et al., 2017; Zhou et al., 2022). However, so far there has been limited
49 research that specifically identifies occurrences of quasi-balanced subsurface vertical velocity and examines how turbulence
50 responds to such instances.

51 Vertical motion at fronts is driven by frontogenesis, instability processes, nonlinear Ekman effects, and
52 filamentogenesis (Klein and Lapeyre, 2009; Mahadevan, 2016; Mahadevan et al., 2020a; McWilliams, 2021; Capó and
53 McWilliams, 2022; Garcia-Jove et al., 2022). Instabilities have also been identified as a key source of turbulence and energy
54 dissipation at oceanic fronts (D'Asaro et al., 2011; Carpenter et al., 2020; McWilliams, 2021). Subsurface intrusions carry
55 physical (temperature and salinity) and biogeochemical properties (oxygen and chlorophyll-a) characteristic of the surface
56 mixed layer along isopycnals and extend downward and laterally. Intrusions are often identified because of the co-occurrence
57 of subsurface maxima in oxygen, particulate organic carbon with anomalous temperature and salinity properties (i.e., spice;
58 Omand et al., 2015). Intermittent intrusions subducting along the outer periphery of mesoscale and submesoscale structures
59 have previously been identified (Johnston et al., 2011; Llorc et al., 2018; Chapman et al., 2020; Johnson and Omand, 2021;
60 Chen et al., 2021; Capó and McWilliams, 2022; Freilich et al., 2024). This study measures the turbulent erosion of a subducting
61 intrusion at fronts within the Western Alboran Gyre (WAG), a major mesoscale feature in the western Mediterranean Sea.
62 Data were collected in the framework of the Coherent Lagrangian Pathways from the Surface Ocean to Interior (CALYPSO)
63 project onboard the R/V *Pourquois Pas?*, that aimed to examine subduction features in close proximity to the unstable front
64 that developed along the northern edge of the WAG (Mahadevan et al., 2020).



65 Previous studies have investigated turbulence data collected with microstructure probes in both the surface (Cuypers
66 et al., 2012; Forryan et al., 2012; Vladioiu et al., 2021) and deep (Ferron et al., 2021; van Haren, 2023) regions of the Western
67 Mediterranean Sea. However, this work represents the first comprehensive investigation of turbulence in a context of
68 mesoscale-submesoscale subduction at frontal zones within the WAG. This paper begins with a comprehensive description of
69 water column properties and a turbulence dataset. We then conduct an examination of physical and biogeochemical properties
70 across frontal transects to identify and characterize subducting features. Finally, we calculate the turbulent erosion of a selected
71 intrusion of interest.

72 **2 Material and methods**

73 **2.1 Sampling strategy and profile inventory**

74 The study zone is highly dynamic and significantly influenced by the eastward-flowing Atlantic jet that sustains the WAG
75 (Sánchez-Garrido and Nadal, 2022). The jet is characterized by a pronounced frontal zone, exhibiting a density contrast of up
76 to 1.0 kg m^{-3} at its boundaries (Oguz et al., 2014).

77 We conducted five transects across the salinity front identified through operational modeling and satellite estimations
78 in the northern edge of the WAG between March 28th and April 4th 2019 (**Fig. 1B**). Temperature and salinity conditions in the
79 upper water column were sampled, resulting in a total of 136 profiles (mean depth: 231 m). Turbulence data were collected on
80 43 stations (mean depth: 219 m) during the campaign. With the exception of a single station, all stations featured duplicate
81 microstructure profiles, from which the mean value between these replicates was computed. Furthermore, we obtained 22
82 dissolved oxygen and chlorophyll-a profiles (mean depth: 284 m) concurrently with the microstructure profiles.

83 **2.2. Temperature, salinity and derived variables**

84 Temperature and salinity data were acquired using a Teledyne RD Instruments Underway Conductivity Temperature Depth
85 (UCTD) profiler, as detailed by Rudnick and Klinke (2007). The sampling rate is 16 Hz, with the UCTD falling velocity
86 ranging between 1.5 and 3.5 m s^{-1} . The spatial resolution between UCTD cycles was approximately 1 km, given a cruise speed
87 of 3 m s^{-1} knots during recovery. The UCTD downcasts were post-processed for sensor alignment, salinity spikes correction
88 and were binned using a spline interpolation onto a vertical grid of 1 m. A comprehensive description of data post-processing
89 procedures can be found in Dever et al., (2019). Key oceanographic parameters, including absolute salinity, conservative
90 temperature, Brunt–Väisälä frequency (N^2), density ratio and Turner angle and spice were computed using the Gibbs Sea
91 Water oceanographic toolbox of TEOS-10 (<https://www.teos-10.org/pubs/gsw>).

92 N^2 serves as an indicator of water column vertical stability and was determined using equation (1):

$$93 \quad N^2 = -\frac{g}{\rho_w} \frac{\partial \rho}{\partial z} \quad (1)$$



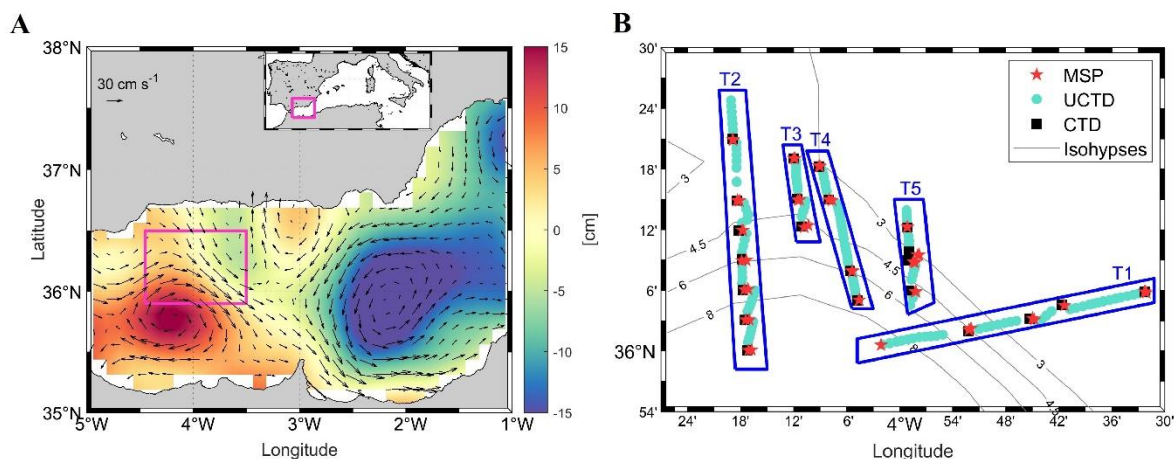
94 where g represents gravitational acceleration (9.8 ms^{-2}), ρ_w is a reference seawater density (1025 kg m^{-3}), and $\partial\rho/\partial z$ denotes
95 the variability of potential density with depth. The density ratio quantifies the vertical contributions of conservative
96 temperature and absolute salinity to the stability of the water column (following the Thermodynamic Equation of Seawater –
97 2010; IOC et al., 2010). The Turner angle, as outlined by McDougall et al., (1988), was computed to identify water column
98 conditions, including double diffusivity (thermal diffusivity or salt fingering), stability, and instability regimes. Seawater spice,
99 defined as the temperature and salinity variability along isopycnals, was employed to discern water masses with similar density,
100 but varying temperature and salinity characteristics (McDougall et al., 2021). Spice anomaly was computed with respect to the
101 mean spice profile computed in a temperature-salinity space and obtained including all spice profiles of the dataset.
102 Furthermore, mixed layer depth was determined using a density threshold of 0.03 kg m^{-3} relative to the reference density at 10
103 m depth, as proposed by de Boyer Montégut et al. (2004). Isopycnal strain, which measures the stretching or compression of
104 isopycnal surfaces, was calculated as the vertical gradient of isopycnal displacement (Pinkel et al., 1991). This displacement
105 is defined as the difference between the actual depth of each isopycnal and its expected depth based on the mean density
106 profile.

107 **2.3. Detection of subducting intrusions**

108 Observational evidence of water being subducted from the upper ocean layer to below the mixed layer was observed by
109 leveraging the high spatio-temporal resolution of the underway data collected by the UCTD. The presence of subsurface
110 intrusions in a frontal transect was semi-automatically detected from the vertical profiles, based on subsurface spice and
111 temperature anomalies. The detection algorithm proceeds as follows: I) Compute average spice on isopycnals for the campaign
112 (auto). II) Compute spice anomaly on an isopycnal for each profile phase (auto). III) Detect subsurface anomalies in spice
113 anomaly using a peak-finding algorithm based on peak prominence (auto). IV) Retain anomalies with at least 5 samples (i.e.,
114 1.5 m; auto) and occur coherently over more than 3 consecutive profiles (manual).

115

116



117

118 **Figure 1.** (A) Map of the Alboran Sea showing the mean absolute dynamic topography (colors) and geostrophic currents (arrows) on March
119 30th-31st, 2019. The purple inset shows the location of the sampling effort, detailed in panel (B), where blue rectangles denote the sampling
120 stations selected for transect (T#) analysis. T1 was realized on March 29th, T2 on March 30th and T3-T5 on March 31st. Isohypsies of absolute
121 dynamic topography are depicted as gray lines. Red stars, cyan circles and black squares correspond to sampling stations for the
122 microstructure profiler, underway CTD and CTD, respectively. Daily absolute dynamic topography and geostrophic current data were
123 downloaded from <https://data.marine.copernicus.eu/>.

124

125 2.4. Dissolved oxygen and Chlorophyll-a

126 We equipped a SeaBird 911plus CTD probe with a SeaBird 43 dissolved oxygen sensor and a WET Labs ECO-AFL/FL
127 fluorometer to assess dissolved oxygen and chlorophyll-a concentrations, respectively. The CTD data underwent bin-averaging
128 to achieve a vertical resolution of 0.5 m and was subsequently calibrated using in situ data. Dissolved oxygen estimates were
129 aligned with measurements obtained through Winkler titration ($n = 67$; Mahadevan et al., 2020b), while chlorophyll-a estimates
130 derived from fluorescence were calibrated against data from fluorometric determinations ($n = 140$; Alou-Font et al., 2019). A
131 high level of agreement was found between in situ measurements and CTD-derived estimations, as evidenced by coefficient
132 of determination (R^2) values of 0.99 for dissolved oxygen and 0.85 for chlorophyll-a.

133 Oxygen and chlorophyll-a anomaly on isopycnals were computed following equation (2):

$$134 X_a = X_\rho - \bar{X}_\rho \quad (2)$$

135 where X_a represents the variable (i.e., oxygen or chlorophyll-a) anomaly, X_ρ denotes the observed value at a specific density
136 and \bar{X}_ρ is the mean property value corresponding to this density.

137 2.5. Horizontal ocean currents

138 Horizontal current magnitude and direction were collected using a hull-mounted Teledyne RDI Ocean Surveyor Acoustic
139 Doppler Current Profiler (ADCP) operating at a frequency of 150 kHz and with a vertical bin size of 4 m. Detailed post-
140 processing procedures for ADCP data have been exhaustively documented in Mahadevan et al. (2020b) and Cutolo et al.



141 (2022). Shear squared was calculated from ADCP data as the sum of the squares of the vertical gradients of the horizontal
142 velocity components (Gregg, 1989).

143 2.6. Turbulent kinetic energy dissipation rates

144 Various methods have been employed to quantify turbulent mixing (e.g., integral approaches, finescale parameterizations and
145 direct microstructure measurements; Thorpe, 2005; Shroyer et al., 2018). In this study, we present turbulence dissipation rates
146 observations and derived parameters (Thorpe, 2005) collected using a free-falling microstructure profiler (MSS90D; Sea &
147 Sun Technology). The probe was equipped with two microstructure shear sensors (PNS6), with the final turbulent dissipation
148 rate calculated as the mean of the two shear probe estimates. The profiler's buoyancy was adjusted to achieve a sinking velocity
149 between 0.6 and 0.7 m s⁻¹ and the data sampling occurred at a frequency of 1024 Hz but was internally averaged to 512 Hz to
150 comply with signal degradation along the 1.2 km probe cable. Post-processing and turbulent dissipation rate calculations were
151 carried out using the microstructure profiler processing toolbox developed by Schultz et al. (2022). We fine-tuned instrument-
152 specific parameters according to the microstructure profiler employed in this study (e.g., sampling frequency, sensors
153 calibration and sensitivity, distance of other sensors to the shear sensor's tip), while the threshold parameters for data validation
154 from Schultz et al. (2022) were retained.

155 Kinetic energy dissipation rates (ϵ) were computed as per equation (3):

$$156 \epsilon = 15\nu \overline{\left(\frac{\partial u}{\partial z}\right)^2} \quad (3)$$

157 where ν represents the kinematic molecular viscosity and $\overline{(\partial u/\partial z)^2}$ is the spatial average of vertical shear variation with depth
158 (Taylor, 1935). Turbulent dissipation rates from both shear probes were treated separately, averaging all shear spectra within
159 1 m vertical bin. The shear spectrum results were iteratively fitted to the Nasmyth (Nasmyth, 1970) reference shear spectrum
160 and the deviation of the observed spectrum with respect to the Nasmyth's was used for data quality check. A detailed
161 description of the data processing procedure was described in Schultz et al. (2022). We performed data-averaging at 1-meter
162 depth intervals, excluding the initial 15 meters of each profile, to mitigate the noise arising from ship motion and wave-
163 breaking (D'Asaro, 2014).

164 The microstructure data exhibited good agreement ($R^2 = 0.89$) between the two shear sensors ($n=8957$;
165 **Supplementary Fig. 1A**), with a stronger correlation observed under elevated turbulence conditions ($\epsilon > 10^{-7} \text{ W kg}^{-1}$) compared
166 to calmer waters ($\epsilon < 10^{-7} \text{ W kg}^{-1}$). Another quality control parameter was the magnitude of the pseudo dissipation rates
167 originated from the profiler high frequency vibrations, consistently one order of magnitude lower than turbulent kinetic energy
168 dissipation rates (**Supplementary Fig. 1B**) and predominantly (36.9%) falling within the range of $1.0 \cdot 10^{-10}$ to $1.6 \cdot 10^{-10} \text{ W kg}^{-1}$.
169

170 2.7 Turbulent fluxes

171 Vertical diffusivity (K_z) is computed according to equation (4):



172 $K_z = \gamma \frac{\varepsilon}{N^2}$ (4)

173 where the mixing efficiency is $\gamma = 0.2$ (Gregg et al., 2018; Mouriño-Carballido et al., 2021; Lozovatsky et al., 2022), ε is the
174 turbulent kinetic energy dissipation rate and N^2 denotes the squared buoyancy frequency.

175 We determine turbulent heat (in units of W m^{-2}) and salt fluxes ($\text{kg m}^{-2} \text{s}^{-1}$) following Sheehan et al. (2023) and
176 equations (5) and (6):

177 $Q_H = -\rho C_p K_z \frac{\partial \theta}{\partial z}$ (5)

178 $Q_S = 10^{-3} \left(-\rho K_z \frac{\partial S}{\partial z} \right)$ (6)

179 where ρ is seawater density, C_p is the specific heat capacity of seawater ($3850 \text{ J kg}^{-1} \text{ }^\circ\text{C}^{-1}$), $\partial\theta/\partial z$ corresponds to the vertical
180 gradient of conservative temperature, and $\partial S/\partial z$ indicates the vertical gradient of absolute salinity. Furthermore, turbulent
181 fluxes of dissolved oxygen and chlorophyll-a (in units of $\text{mg m}^{-2} \text{s}^{-1}$) were estimated using equations (7) proposed by Williams
182 et al. (2013):

183 $Q_X = -K_z \frac{\partial X}{\partial z}$ (7)

184 where ∂X denote the variable (i.e., oxygen or chlorophyll-a) vertical gradient with depth.

185 Our analysis primarily focused on the subducting intrusion identified along transect 2 during the 2019 CALYPSO
186 campaign (**Fig. 1B**). The limited number of microstructure profiles precluded a comprehensive analysis of spatiotemporal
187 intrusions variability along the other transects. To assess the physical and biogeochemical conditions around the subducting
188 intrusion boundaries, we calculated the mean conditions within 5 m inside and outside the intrusion boundaries.

189 3 Results

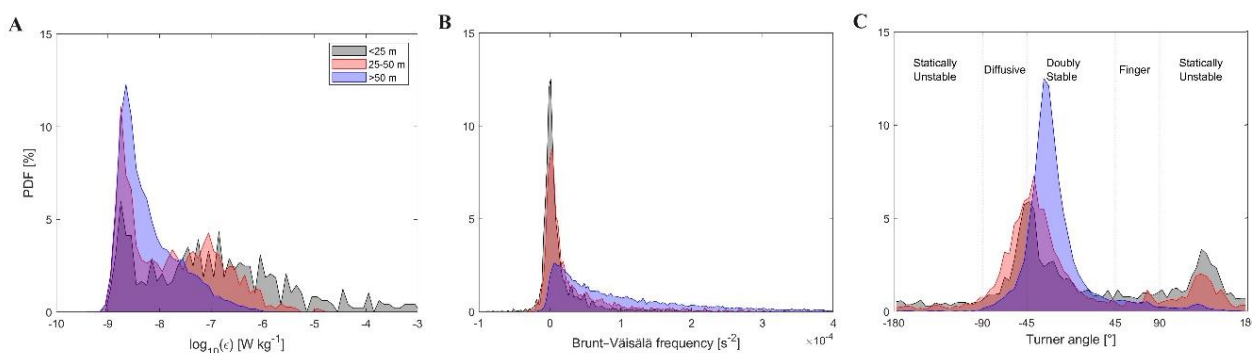
190 3.1 Water column stability and turbulent kinetic energy

191 High mixing was observed in the surface layer, with localized turbulence peaks in the subsurface water column. Turbulent
192 kinetic energy (TKE) values displayed considerable variability, with 43.8% of observations falling between $1.3 \cdot 10^{-9}$ and $4.0 \cdot 10^{-9}$
193 W kg^{-1} (mean \pm standard deviation: $8.2 \cdot 10^{-9} \pm 2.4 \cdot 10^{-8} \text{ W kg}^{-1}$), with a peak (11.2%) identified in the range of $2.0 \cdot 10^{-9}$ to
194 $2.5 \cdot 10^{-9} \text{ W kg}^{-1}$. An analysis of ε probability distribution by depth intervals indicated that 95% of deep ε values were comprised
195 between 10^{-9} and $10^{-7} \text{ W kg}^{-1}$ (**Fig. 2A**). In contrast, surface and mid-water depths exhibited a lower proportion (53% and 77%,
196 respectively) within this ε range. Surface waters ($<25 \text{ m}$) were characterized by elevated ε values, with 25% and 12% of the
197 data falling within the ranges of 10^{-7} - 10^{-6} and 10^{-6} - $10^{-5} \text{ W kg}^{-1}$, respectively.

198 Elevated homogeneity in the shallow water column vertical structure was observed. Indeed, the probability
199 distribution of Brunt–Väisälä frequency (N^2) by depth intervals (**Fig. 2B**) indicated lower stratification in the surface and mid-
200 water layers, where approximately 81% and 67% of values were lower than $0.2 \cdot 10^{-4} \text{ s}^{-2}$, respectively. Conversely, the deeper
201 portion ($>50 \text{ m}$) of the water column exhibited stronger stratification, with an increased proportion (70%) of N^2 estimations



202 exceeding $0.3 \cdot 10^{-4} \text{ s}^{-2}$. These patterns were reflected in water column regimes. Examination of Turner angle values revealed a
 203 predominantly stable water column, accounting for 74% of the dataset (**Fig. 2C**). However, these stability conditions exhibited
 204 notable variations with depth. The shallow layer displayed a more varied scenario with a near-equal distribution between
 205 statically unstable and doubly stable conditions. In contrast, the mid-water column featured the highest proportion (27%) of
 206 diffusive regimes and the deep layer was primarily characterized (83%) by double stable conditions.



207

208 **Figure 2.** Probability distribution frequency (PDF) by depth intervals for turbulent kinetic energy dissipation rates (A), Brunt-Väisälä
 209 frequency (B) and Turner angle values (C). Colored shaded areas in panels correspond to different depth intervals, with gray: 15-25 m; red:
 210 26-50 m; blue: depths >51 m. The names in panel (C) reflect the water column regime according to the Turner angle value (McDougall et
 211 al., 1988).

212

213 3.2 Transects across the Western Alboran Gyre front

214 A noticeable depression in the isopycnals was consistently observed in all the transects extending towards the interior of the
 215 anticyclone (**Fig. 3** and **Supplementary Fig. 2-6**). The highest ϵ below the mixed layer was detected adjacent to zones featuring
 216 elevated vertical density gradients and deepening along the isopycnals in transects 2 (**Fig. 3**). A deepening of positive spice
 217 anomalies from approximately 50 to 100 m was observed at the start of transect 1 and from 15-35 km of transect 2. Subducting
 218 intrusions were observed along all transects, except for transect 3, possibly owing to its shorter length (approximately 12 km;
 219 **Fig. 3** and **Supplementary Fig. 2-6**). The mean thickness of subducting intrusions was computed at 14.2 m (standard deviation:
 220 9.4 m), ranging from a minimum of 1.7 to a maximum of 42.2 m.

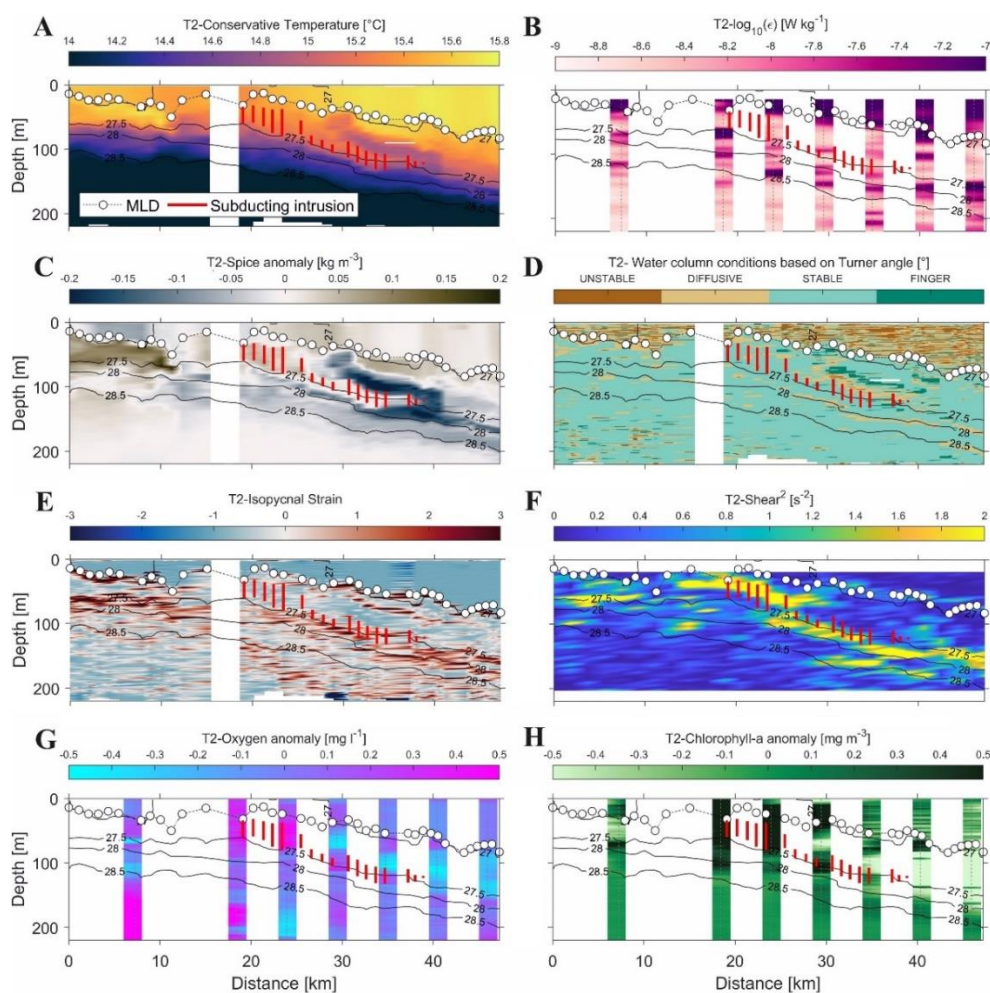
221 The subduction is likely occurring along the front and not necessarily along the tilted isopycnal. Enhanced ϵ and
 222 diffusivity values were noted in proximity to the base of the mixed layer and in the vicinity of subducting intrusion boundaries
 223 (**Fig. 4**). Furthermore, diffusive water column conditions were identified along the upper boundary of the subducting intrusion
 224 in transect 2 (**Fig. 3D**) and adjacent to the subducting intrusions within transects 1 and 4. Positive isopycnal strain values were
 225 observed at both edges of the subducting intrusion initially, with a predominant concentration of positive values indicating
 226 stretching of isopycnal surfaces primarily at the bottom edge as subduction progressed. The current data along transect 2
 227 illustrated a horizontal velocity magnitude exceeding 60 cm s^{-1} within the interior of the anticyclone, while lower values were
 228 observed on its periphery. The subducting intrusion, identified beneath the superficial high-velocity patch and within a zone



229 of elevated shear squared (primarily due to a negative vertical gradient of the zonal velocity component; **Fig. 3**), was
230 characterized by a horizontal velocity estimated at approximately 0.5 m s^{-1} .

231 A deepening of the well oxygenated surface layer towards the center of the anticyclone was observed in transects 1
232 and 2 (**Supplementary Fig. 2** and **Fig. 3**, respectively). Elevated dissolved oxygen anomaly concentrations ($>0.5 \text{ mg l}^{-1}$) were
233 detected inside the subducting intrusion along transect 2 (**Fig. 3**), with high values deepening from approximately 50 to 120
234 m. Similarly, anomalous high chlorophyll-a anomaly values were found near the 30 km of transect 2, with anomaly
235 concentrations of up to 1.4 mg m^{-3} detected at a depth of 100 m.

236
237

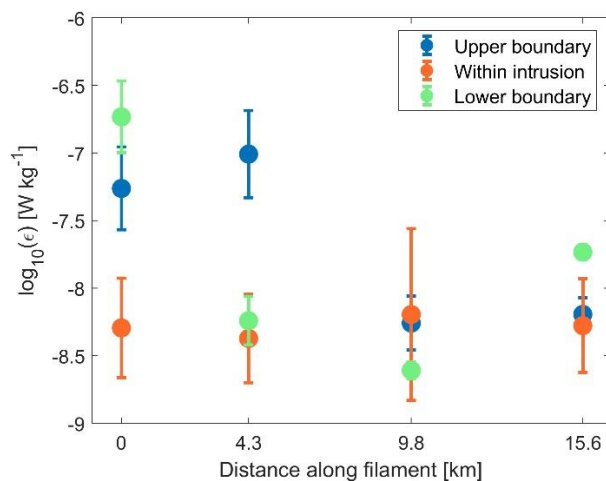


238

239 **Figure 3.** Profiles of conservative temperature (A), turbulent kinetic energy dissipation rates (B), spice anomaly (C), water column conditions
240 based on Turner angle estimations (D), isopycnal strain (E), share squared (F), dissolved oxygen anomaly (G), and chlorophyll-a anomaly
241 (H) estimations acquired along transect 2 of the 2019 CALYSPSO campaign. Isopycnals are represented as black lines, while the mixed
242 layer depth and subducting intrusions are denoted by colored points and lines, respectively. The distances between stations were calculated
243 starting from the northernmost sampling point.



244



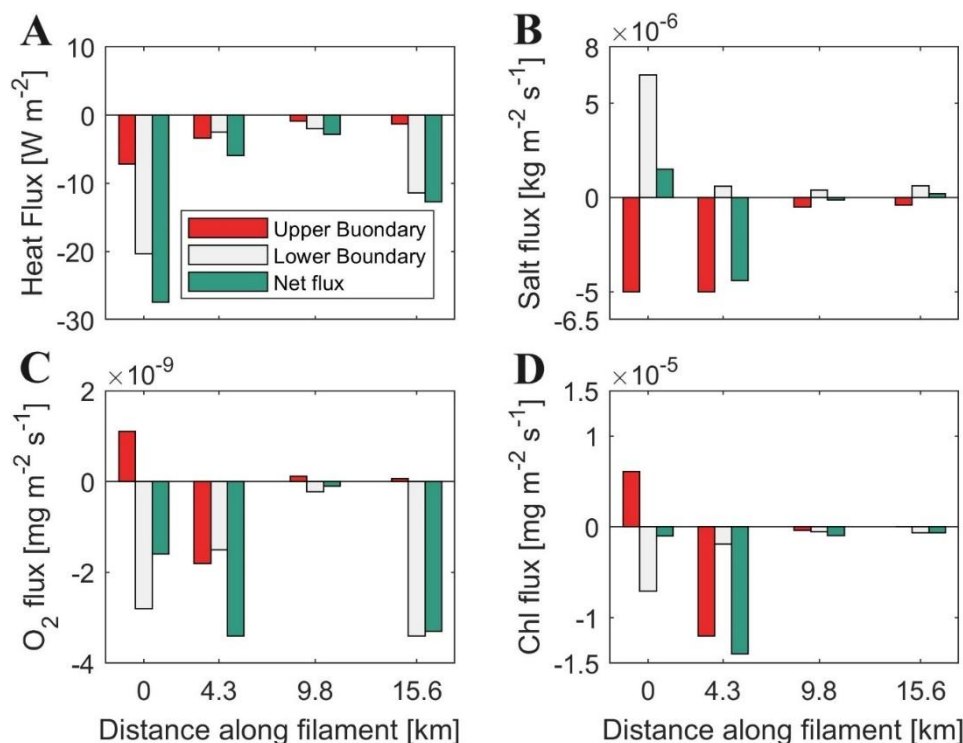
245

246 **Figure 4.** Mean turbulent kinetic energy values within the intrusion and at its upper and lower boundaries (5 m from the intrusion edges).
247 The errorbars represent the measurement standard deviation.

248

249 3.3 Turbulent fluxes around the subducting intrusion

250 We focused our analysis of the microstructure profiles to transect 2 during the 2019 CALYPSO campaign due to its higher
251 horizontal resolution (**Fig. 1B**). Turbulent fluxes within the interior of the transect 2 intrusion exhibited reduced values
252 compared to water column around both intrusion edges (**Supplementary Fig. 7**). Notably, turbulent fluxes exhibited higher
253 magnitudes within the first two profiles sampling the edges of the subducting intrusion in comparison to the subsequent two
254 profiles (**Fig. 5**). Turbulent fluxes around the intrusion boundaries resulted in a net loss of heat, oxygen and chlorophyll-a
255 properties from within the intrusion to the surrounding ocean, while salinity increased (**Table 1**). Heat, oxygen and chlorophyll-
256 a turbulent fluxes exhibited negative values (i.e., indicating downward direction) at the base of the intrusion, while salt fluxes
257 displayed positive values (i.e., upward direction) at both boundaries of the intrusion. Positive heat flux values were consistently
258 recorded near the upper intrusion boundary at all sampling stations, although more variability was observed in oxygen and
259 chlorophyll-a fluxes. The mean absolute values for turbulent fluxes indicated reduced heat, oxygen and chlorophyll-a fluxes
260 near the upper boundary in contrast to the intrusion's base. Specifically, the upper heat flux accounted for only 35% of the
261 magnitude observed near the base of the intrusion, while the upper oxygen and chlorophyll-a fluxes represented 68 and 63%,
262 respectively, of the corresponding bottom flux magnitude. The fluxes uncertainty was provided in **Supplementary Table 1**.



263

264 **Figure 5.** Estimations of turbulent fluxes of heat (A), salt (B), oxygen (C) and chlorophyll-a (D) along the upper and lower boundaries of
 265 the subducting intrusion identified within transect T2 of the 2019 CALYPSO campaign and the resulting net flux (in green). The distances
 266 between the four stations where the fluxes were calculated (as shown in Supplementary Figure 7) along the subducting intrusion are provided.
 267 Positive (negative) values for the turbulent fluxes represent a gain (loss) of the respective variables within the interior of the intrusion.

268

269

270 **Table 1.** Mean (\pm 95% confidence interval) conservative temperature, absolute salinity, dissolved oxygen and chlorophyll-a conditions
 271 within the subducting intrusion identified along transect T2. The distances between the four stations, the intrusion mean depth and thickness
 272 are provided.

273

Distance	Depth	Thickness	Temperature	Salinity	Oxygen	Chlorophyll-a
[km]	[m]	[m]	[°C]	[g kg ⁻¹]	[mg l ⁻¹]	[mg m ⁻³]
0	47	25.9	15.28 \pm 0.05	37.03 \pm 0.03	7.74 \pm 0.07	1.81 \pm 0.12
4.3	59	42.2	15.27 \pm 0.06	37.04 \pm 0.04	7.84 \pm 0.10	2.16 \pm 0.28
9.8	99	13.3	15.16 \pm 0.03	37.10 \pm 0.03	7.43 \pm 0.05	1.38 \pm 0.13
15.6	120	24.9	14.91 \pm 0.06	37.15 \pm 0.07	7.16 \pm 0.04	0.68 \pm 0.02

274



275 4 Discussion

276 4.1 Turbulent kinetic energy dissipation rates in the Western Alboran Sea

277 The TKE dissipation rates in our study were (mean: $8.2 \cdot 10^{-9} \text{ W kg}^{-1}$) found to be comparable to those reported in previous
278 investigations involving microstructure data in the Mediterranean Sea. For instance, Cuypers et al. (2012) calculated mean
279 TKE values of approximately $10^{-8} \text{ W kg}^{-1}$ below the seasonal pycnocline. Our TKE estimates unveiled an intermediate
280 turbulent environment, between the Mediterranean energetic and quiescent regions (mean: $5.2 \cdot 10^{-8}$ and $4.7 \cdot 10^{-10} \text{ W kg}^{-1}$,
281 respectively; Vladioiu et al., 2021). Interestingly, our findings exhibited a closer resemblance to the TKE observed west of the
282 Gibraltar Strait, where the mean TKE was $4 \cdot 10^{-9} \text{ W kg}^{-1}$ in the ocean interior (Fernández-Castro et al., 2014).

283 The observed peaks in TKE dissipation rates were predictably situated in shallow ocean regions influenced by wave
284 breaking, in close proximity to the base of mixed layer (Zippel et al., 2022) and near the boundaries of subducting intrusions
285 (**Fig. 3**). However, other peaks were detected at deeper levels and did not appear to correlate with aforementioned factors.
286 Mixing processes in the stratified ocean below the mixed layer are often attributed to vertical shear extending below the MLD,
287 penetrative convection and the breaking of internal waves (MacKinnon et al., 2013). The Western Alboran Sea may be
288 influenced by the eastward propagation of internal waves traveling along isopycnals generated by the interaction of tidal
289 currents with bathymetry at the Gibraltar Strait (Thorpe, 2007; Alpers et al., 2008; Bolado-Penagos et al., 2023). While
290 symmetric instabilities have been identified as effective mechanisms for geostrophic energy dissipation in the ocean interior
291 (Zhou et al., 2022), the positive sign of the potential vorticity associated with subducting water in the study area (Freilich and
292 Mahadevan, 2021) suggests that the conditions required for this process to occur may not be met. Another plausible explanation
293 for the deep TKE peaks could be provided by dissipation associated with subducting intrusions that may have gone undetected
294 by our methodology. Conducting future surveys with mooring and/or glider deployments to identify internal waves within the
295 study zone could significantly advance our comprehension of their spatiotemporal variability and their role in generating deep
296 turbulence along isopycnals.

297 4.2 Water column regimes

298 The convergence of Atlantic and Mediterranean waters in the study zone resulted in a robust stratification of the water column,
299 characterized predominantly by doubly stable conditions. Along isopycnals and at the upper boundary of the subducting
300 intrusion (**Figure 3**), we observed instances of diffusive convection regimes. While diffusive convection is typically associated
301 with thermohaline staircases and is more commonly found at higher latitudes (Kelley et al., 2002; van der Boog et al., 2021),
302 the presence of horizontal variability in temperature and salinity conditions in our study area may lead to the formation of
303 coherent subducting intrusions associated with double diffusive convection (Kelley et al., 2002; Schmitt, 2009). Freilich and
304 Mahadevan (2021) proposed that the specific pathway of subducting intrusions along isopycnals in the study zone could be
305 generated by a combination of mesoscale (geostrophic) frontogenesis and submesoscale (ageostrophic) dynamics.



306 The subducting intrusion transports subsurface water column properties into the deeper ocean, undergoing erosion
307 along its pathway through a combination of turbulent and diffusive mixing. This dynamic process results in a modification of
308 its inherent properties.

309 **4.3 Turbulent erosion of the intrusion**

310 The elevated TKE diffusivity rates in the surface layer, coupled with an increase in stratification with depth can potentially
311 account for the higher diffusivity and turbulent fluxes observed at the start of the intrusion's subduction compared to stations
312 sampled further along the subduction path. Moreover, physical and biogeochemical properties of the subducted water
313 resembled surface conditions more closely than those of the deep layer, resulting in reduced fluxes along the upper boundary
314 of the intrusion compared to the lower boundary (with the exception of the station located at 4.3 km).

315 The turbulent erosion of the subducting filament led to an overall decrease in temperature, oxygen and chlorophyll-a
316 content within the filament, while salinity increased (**Table 1**). The slight increment in oxygen and chlorophyll-a concentration
317 observed at the second station within the intrusion may be attributed to either downward fluxes detected at the first station,
318 indicating a supply of biogeochemical properties from the surface layer into the intrusion interior, or in situ phytoplankton
319 production (the photic layer was estimated to be around 60 m deep; **Supplementary Fig. 8**).

320 However, these diapycnal fluxes were too weak to induce a significant dilution of the intrusion, as daily fluxes
321 (**Supplementary Table 2**) were orders of magnitude smaller than the mean property values within the intrusion. These
322 estimates did not account for double-diffusive mixing fluxes characteristic of thermohaline staircases, as such features are
323 predominant at greater depths in the Western Mediterranean Sea (Onken and Brambilla, 2003; Schroeder et al., 2016; Ferron
324 et al., 2021). Along the upper boundary of the intrusion, diffusive convection regimes were identified, resulting from the
325 subduction of warmer and less saline water by the intrusion. Despite of this, an estimate of diffusive convection mixing
326 indicated that these fluxes were generally an order of magnitude lower than turbulent fluxes, suggesting a limited impact on
327 intrusion dilution or enrichment (**Supplementary Table 2**).

328 In addition to turbulent and diffusive convection mixing, various factors contribute to the typical vertical variability
329 in ocean temperature and salinity. These factors include the attenuation of solar irradiation, the evaporation-precipitation
330 budget, water column density stability and isopycnal mixing. Conversely, the decline in oxygen and chlorophyll-a content with
331 depth can be attributed to the deepening of the photic layer, distance from the atmospheric-ocean boundary layer, and processes
332 such as remineralization, respiration, and grazing. The modification of the typical vertical variability in biogeochemical
333 properties induced by subducting intrusions might have profound impacts on ecosystem dynamics within the study zone.

334 **4.4 Biogeochemical significance of subducting intrusions**

335 The Atlantic Jet, which enters the Mediterranean through the Strait of Gibraltar, coupled with coastal upwelling events,
336 transforms our study area into one of the most productive zones in the Mediterranean despite the Mediterranean Sea's well-
337 known status as an oligotrophic basin (Reale et al., 2020; Sánchez-Garrido and Nadal, 2022). The outer boundary of the WAG



338 has also been identified as a stirring region where properties of the water column are continually exchanged as they are advected
339 towards the center of the anticyclone (Brett et al., 2020; Sala et al., 2022). Subduction of the intrusion may enhance particulate
340 organic carbon export below the mixed layer, reducing its exposure time to remineralization (Freilich et al., 2024). This process
341 contributes to one of the highest export rates observed in the Mediterranean Sea based on sediment trap and particle size
342 distribution profiles data (Ramondenc et al., 2016). Additionally, the mixing associated with subducting intrusions may
343 facilitate the reorganization of phytoplankton communities, traditionally stratified in the photic layer (Mena et al., 2019) and
344 their proliferation. This is especially significant, as nitrates are nearly depleted in the shallow layer north of the WAG (Oguz
345 et al., 2014; Lazzari et al., 2016; García-Martínez et al., 2018). It has been demonstrated that oceanic fronts might act as
346 aggregation areas for planktonic organisms, becoming important foraging areas for higher trophic layers (Acha et al., 2015).
347 Moreover, the transport of chlorophyll-a towards the center of the WAG could lead to an increase in the biomass of diel vertical
348 migrant zooplankton, which tends to be more abundant in the inner part of the gyre compared to its periphery (Yebera et al.,
349 2018).

350 **5 Conclusions**

351 The Western Alboran Gyre is a dynamical feature characterized by high spatiotemporal variability arising from the
352 convergence of Mediterranean and Atlantic waters. Indeed, the northern edge of the WAG water column exhibited notable
353 spatial variability in both physical and biogeochemical characteristics. Specifically, the inner part of this gyre featured higher
354 temperature, current velocity, oxygen content and chlorophyll-a concentration compared to its periphery. Moreover, there was
355 an observable deepening of enhanced Brunt–Väisälä frequency and turbulent kinetic energy dissipation rates towards the
356 anticyclone’s center.

357 The investigation of spice anomaly spatial variability allowed the identification of several subducting intrusions
358 occurring beneath the mixed layer depth, extending from the gyre’s outer region towards its center. High turbulent kinetic
359 energy dissipation rates were evident at both the upper and lower boundaries of these intrusions, complemented by localized
360 peaks at deeper levels. The specific factors contributing to these heightened dissipation rates at deeper levels remain elusive.

361 The turbulent fluxes of heat, salt, oxygen and chlorophyll-a along the intrusion boundaries revealed a consistent net
362 loss of physical and biogeochemical properties from within the intrusion to the surrounding ocean. From a biogeochemical
363 perspective, the subduction intrusion holds significance as it has the potential to amplify the export of particulate organic
364 carbon below the mixed layer. Additionally, it may contribute to the enhancement of diel vertical migrant zooplankton biomass
365 and facilitate the proliferation of phytoplankton communities. Notably, mixing due to turbulence or diffusive convection
366 contributed little to the observed variation in temperature, salinity, oxygen or chlorophyll-a within the intrusion interior. Other
367 factors, such as water column density stability, variability of the photic layer depth, and organic matter degradation, likely
368 played a role in these dynamics.



369 While our present study has provided valuable insights into the subduction of intrusions and their turbulent erosion
370 within the Western Alboran Gyre, significant gaps remain in our understanding of the spatiotemporal variability of subducting
371 intrusions. Future targeted surveys that specifically address the persistence and extent of these features might improve
372 quantitative parametrizations of key physical and biogeochemical property subduction. Explorations encompassing a broader
373 surface of the WAG may reveal asymmetries in intrusion subduction between the WAG's edges and offer an estimate of the
374 total subduction occurring within the WAG.

375

376 *Funding.* CALYPSO constitutes a Departmental Research Initiative funded by the U.S. Office of Naval Research. GT was
377 founded by ISMAR-26-2022-VE research fellowship. TMSJ was supported by ONR grant N00014-18-1-2416.

378

379 *Data availability.* Data will be made available on request.

380

381 *Author contributions.* GT: Conceptualization, Methodology, Software, Validation, Formal analysis, Data Curation, Writing -
382 Original Draft, Writing - Review & Editing, Visualization. MD: Methodology, Software, Data Curation, Writing - Original
383 Draft, Writing - Review & Editing, Supervision. MF: Resources, Writing - Review & Editing. AM: Resources, Writing -
384 Review & Editing, Project administration, Funding acquisition. SJ: Resources, Writing - Review & Editing. LP: Resources,
385 Writing - Review & Editing. FF: Conceptualization, Methodology, Software, Data Curation, Writing - Original Draft, Writing
386 - Review & Editing, Supervision, Project administration, Funding acquisition.

387

388 *Competing interests.* The authors declare that they have no conflict of interest.

389

390 *Acknowledgements.* We extend our sincere appreciation to the captains and crews of the R/V *Pourquois Pas?*, as well as the
391 technical and scientific personnel involved in making measurements and providing support. The authors wish to express their
392 gratitude to Leo Middleton engaging in insightful conversations that influenced the development of this article. Furthermore,
393 we would like to acknowledge all the CALYPSO researchers whose constructive comments during CALYPSO's Padua
394 meeting enriched this study.

395

396 **References**

397 Acha, E. M., Piola, A., Iribarne, O., and Mianzan, H (Eds.): Ecological processes at marine fronts: Oases in the ocean,
398 Springer, Berlin, Germany, 68 pp., ISBN 978-3-319-15479-4, 2015.

399 Alou-Font, M., Carbonero, A., and Allen, J.: NRV Alliance report on delayed mode calibration of chlorophyll data.
400 CALYPSO19 cruise 28-03/10-04/19 V-1.0.0, SOCIB-Biogeochemistry Tech. Rep., 2019.



- 401 Alpers, W., Brandt, P., and Rubino, A.: Internal waves generated in the Straits of Gibraltar and Messina: Observations from
402 space, in: *Remote Sensing of the European Seas*, Springer Netherlands, 319–330, [https://doi.org/10.1007/978-1-4020-](https://doi.org/10.1007/978-1-4020-6772-3_24)
403 [6772-3_24](https://doi.org/10.1007/978-1-4020-6772-3_24), 2008.
- 404 Bachman, S. D., Fox-Kemper, B., Taylor, J. R., and Thomas, L. N.: Parameterization of frontal symmetric instabilities. I:
405 Theory for resolved fronts, *Ocean Model.*, 109, 72–95, <https://doi.org/10.1016/j.ocemod.2016.12.003>, 2017.
- 406 Barral, Q. B., Zakardjian, B., Dumas, F., Garreau, P., Testor, P., and Beuvier, J.: Characterization of fronts in the Western
407 Mediterranean with a special focus on the North Balearic Front, *Prog. Oceanogr.*, 197, 102636,
408 <https://doi.org/10.1016/j.pocean.2021.102636>, 2021.
- 409 Belkin, I. M., and Cornillon, P. C.: Fronts in the world ocean’s Large Marine Ecosystems, In: *International Council for the*
410 *Exploration of the Sea, Annual Science Conference*, Helsinki, Finland. CM 2007/D:21, 33 pp., 2007.
- 411 Bolado-Penagos, M., Sala, I., Jesús Gomiz-Pascual, J., González, C. J., Izquierdo, A., Álvarez, Ó., Vázquez, Á., Bruno, M.,
412 and van Haren, H.: Analysis of internal soliton signals and their eastward propagation in the Alboran Sea: exploring the
413 effect of subinertial forcing and fortnightly variability, *Prog. Oceanogr.*, 217, 103077,
414 <https://doi.org/10.1016/j.pocean.2023.103077>, 2023.
- 415 Bonaduce, A., Cipollone, A., Johannessen, J. A., Staneva, J., Raj, R. P., and Aydogdu, A.: Ocean mesoscale variability: a case
416 study on the Mediterranean sea from a re-analysis perspective, *Front. Earth Sci.*, 9, 816,
417 <https://doi.org/10.3389/feart.2021.724879>, 2021.
- 418 Brett, G. J., Pratt, L. J., Rypina, I. I., and Sánchez-Garrido, J. C.: The western Alboran gyre: An analysis of its properties and
419 its exchange with surrounding water, *J. Phys. Oceanogr.*, 50, 3379–3402, <https://doi.org/10.1175/JPO-D-20-0028.1>, 2020.
- 420 Capó, E. and McWilliams, J. C.: Coherent lagrangian pathways near an east Alboran front, *J. Geophys. Res. Ocean.*, 127,
421 e2021JC018022, <https://doi.org/10.1029/2021JC018022>, 2022.
- 422 Capó, E., Orfila, A., Mason, E., and Ruiz, S.: Energy conversion routes in the western Mediterranean sea estimated from eddy-
423 mean flow interactions, *J. Phys. Oceanogr.*, 49, 247–267, <https://doi.org/10.1175/JPO-D-18-0036.1>, 2019.
- 424 Carpenter, J. R., Rodrigues, A., Schultze, L. K. P., Merckelbach, L. M., Suzuki, N., Baschek, B., and Umlauf, L.: Shear
425 Instability and Turbulence Within a Submesoscale Front Following a Storm, *Geophys. Res. Lett.*, 47, e2020GL090365,
426 <https://doi.org/10.1029/2020GL090365>, 2020.
- 427 Chapman, C. C., Lea, M. A., Meyer, A., Sallée, J. B., and Hindell, M.: Defining Southern Ocean fronts and their influence on
428 biological and physical processes in a changing climate, <https://doi.org/10.1038/s41558-020-0705-4>, 24 February 2020.
- 429 Chen, S., Wells, M. L., Huang, R. X., Xue, H., Xi, J., and Chai, F.: Episodic subduction patches in the western North Pacific
430 identified from BGC-Argo float data, *Biogeosciences*, 18, 5539–5554, <https://doi.org/10.5194/bg-18-5539-2021>, 2021.
- 431 Crowe, M. N. and Taylor, J. R.: The evolution of a front in turbulent thermal wind balance. Part 1. Theory, *J. Fluid Mech.*,
432 850, 179–211, <https://doi.org/10.1017/jfm.2018.448>, 2018.
- 433 Cutolo, E., Pascual, A., Ruiz, S., Shaun Johnston, T. M., Freilich, M., Mahadevan, A., Shcherbina, A., Poulain, P. M.,
434 Ozgokmen, T., Centurioni, L. R., Rudnick, D. L., and D’Asaro, E.: Diagnosing Frontal Dynamics From Observations



- 435 Using a Variational Approach, *J. Geophys. Res. Ocean.*, 127, e2021JC018336, <https://doi.org/10.1029/2021JC018336>,
436 2022.
- 437 Cuypers, Y., Bouruet-Aubertot, P., and Marec, C.: Characterization of turbulence from a fine-scale parameterization and
438 microstructure measurements in the Mediterranean Sea during the BOUM experiment, *Biogeosciences*, 9, 3131–3149,
439 <https://doi.org/10.5194/bg-9-3131-2012>, 2012.
- 440 D’asaro, E. A.: Turbulence in the upper-ocean mixed layer, *Ann. Rev. Mar. Sci.*, 6, 101–115, <https://doi.org/10.1146/annurev-marine-010213-135138>, 2014.
- 442 D’Asaro, E., Lee, C., Rainville, L., Harcourt, R., and Thomas, L.: Enhanced turbulence and energy dissipation at ocean fronts,
443 *Science*, 332, 318–322, <https://doi.org/10.1126/science.1201515>, 2011.
- 444 de Boyer Montégut, C., Madec, G., Fischer, A. S., Lazar, A., and Iudicone, D.: Mixed layer depth over the global ocean: An
445 examination of profile data and a profile-based climatology, *J. Geophys. Res. Ocean.*, 109, 1–20,
446 <https://doi.org/10.1029/2004JC002378>, 2004.
- 447 Dever, M., Freilich, M., Hodges, B., Farrar, J., Lanagan, T., and Mahadevan, A.: UCTD and ECOCTD observations from the
448 CALYPSO pilot experiment (2018): Cruise and data report. Woods Hole Oceanographic Institution Tech. Rep., WHOI-
449 2019-01, <https://doi.org/10.1575/1912/23637>, 2019.
- 450 Fedele, G., Mauri, E., Notarstefano, G., and Poulain, P. M.: Characterization of the Atlantic Water and Levantine Intermediate
451 Water in the Mediterranean Sea using 20 years of Argo data, *Ocean Sci.*, 18, 129–142, [https://doi.org/10.5194/os-18-129-](https://doi.org/10.5194/os-18-129-2022)
452 2022, 2022.
- 453 Fernández-Castro, B., Mouriño-Carballido, B., Benítez-Barrios, V. M., Chouciño, P., Fraile-Nuez, E., Graña, R., Piedeleu, M.,
454 and Rodríguez-Santana, A.: Microstructure turbulence and diffusivity parameterization in the tropical and subtropical
455 Atlantic, Pacific and Indian Oceans during the Malaspina 2010 expedition, *Deep. Res. Part I Oceanogr. Res. Pap.*, 94, 15–
456 30, <https://doi.org/10.1016/j.dsr.2014.08.006>, 2014.
- 457 Ferron, B., Bouruet-Aubertot, P., Schroeder, K., Bryden, H. L., Cuypers, Y., and Borghini, M.: Contribution of Thermohaline
458 Staircases to Deep Water Mass Modifications in the Western Mediterranean Sea From Microstructure Observations, *Front.*
459 *Mar. Sci.*, 8, 544, <https://doi.org/10.3389/fmars.2021.664509>, 2021.
- 460 Forryan, A., Allen, J. T., Edhouse, E., Silburn, B., Reeve, K., and Tesi, E.: Turbulent mixing in the eddy transport of Western
461 Mediterranean Intermediate Water to the Alboran Sea, *J. Geophys. Res. Ocean.*, 117, 9008,
462 <https://doi.org/10.1029/2012JC008284>, 2012.
- 463 Freilich, M. A., Poirier, C., Dever, M., Alou-Font, E., Allen, J., Cabornero, A., Sudek, L., Choi, C. J., Ruiz, S., Pascual, A.,
464 Farrar, J. T., Johnston, T. M. S., D’Asaro, E., Worden, A. Z., and Mahadevan, A.: 3D-intrusions transport active surface
465 microbial assemblages to the dark ocean, *bioRxiv*, 121, 2023.09.14.557835, <https://doi.org/10.1073/PNAS.2319937121>,
466 2023.
- 467 Freilich, M. and Mahadevan, A.: Coherent Pathways for Subduction From the Surface Mixed Layer at Ocean Fronts, *J.*
468 *Geophys. Res. Ocean.*, 126, e2020JC017042, <https://doi.org/10.1029/2020JC017042>, 2021.



- 469 Garcia-Jove, M., Moure, B., Zarokanellos, N. D., Lermusiaux, P. F. J., Rudnick, D. L., and Tintoré, J.: Frontal Dynamics in
470 the Alboran Sea: 2. Processes for Vertical Velocities Development, *J. Geophys. Res. Ocean.*, 127, e2021JC017428,
471 <https://doi.org/10.1029/2021JC017428>, 2022.
- 472 García-Martínez, M. del C., Vargas-Yáñez, M., Moya, F., Santiago, R., Muñoz, M., Reul, A., Ramírez, T., and Balbín, R.:
473 Average nutrient and chlorophyll distributions in the western Mediterranean: RADMED project, *Oceanologia*, 61, 143–
474 169, <https://doi.org/10.1016/j.oceano.2018.08.003>, 2019.
- 475 Gregg, M. C.: Scaling turbulent dissipation in the thermocline, *J. Geophys. Res. Ocean.*, 94, 9686–9698,
476 <https://doi.org/10.1029/jc094ic07p09686>, 1989.
- 477 Gregg, M. C., D’Asaro, E. A., Riley, J. J., and Kunze, E.: Mixing efficiency in the ocean, *Ann. Rev. Mar. Sci.*, 10, 443–473,
478 <https://doi.org/10.1146/annurev-marine-121916-063643>, 2018.
- 479 IOC, SCOR, and IAPSO: The international thermodynamic equation of seawater – 2010: Calculation and use of
480 thermodynamic properties. Intergovernmental Oceanographic Commission, Manuals and Guides, 56, UNESCO, 196 pp.,
481 2010.
- 482 Johnson, A. R. and Omand, M. M.: Evolution of a Subducted Carbon-Rich Filament on the Edge of the North Atlantic Gyre,
483 *J. Geophys. Res. Ocean.*, 126, e2020JC016685, <https://doi.org/10.1029/2020JC016685>, 2021.
- 484 Johnston, T. M. S., Rudnick, D. L., and Pallàs-Sanz, E.: Elevated mixing at a front, *J. Geophys. Res. Ocean.*, 116, 11033,
485 <https://doi.org/10.1029/2011JC007192>, 2011.
- 486 Kelley, D. E., Fernando, H. J. S., Gargett, A. E., Tanny, J., and Özsoy, E.: The diffusive regime of double-diffusive convection,
487 *Prog. Oceanogr.*, 56, 461–481, [https://doi.org/10.1016/S0079-6611\(03\)00026-0](https://doi.org/10.1016/S0079-6611(03)00026-0), 2003.
- 488 Klein, P. and Lapeyre, G.: The oceanic vertical pump induced by mesoscale and submesoscale turbulence, *Ann. Rev. Mar.
489 Sci.*, 1, 351–375, <https://doi.org/10.1146/annurev.marine.010908.163704>, 2009.
- 490 Lazzari, P., Solidoro, C., Salon, S., and Bolzon, G.: Spatial variability of phosphate and nitrate in the Mediterranean Sea: A
491 modeling approach, *Deep. Res. Part I Oceanogr. Res. Pap.*, 108, 39–52, <https://doi.org/10.1016/j.dsr.2015.12.006>, 2016.
- 492 Llorc, J., Langlais, C., Matear, R., Moreau, S., Lenton, A., and Strutton, P. G.: Evaluating Southern Ocean Carbon Eddy-Pump
493 From Biogeochemical-Argo Floats, *J. Geophys. Res. Ocean.*, 123, 971–984, <https://doi.org/10.1002/2017JC012861>, 2018.
- 494 Lozovatsky, I. D., Fernando, H. J. S., Jinadasa, S. U. P., and Wijesekera, H. W.: Eddy diffusivity in stratified ocean: a case
495 study in Bay of Bengal, *Environ. Fluid Mech.*, 1–13, <https://doi.org/10.1007/s10652-022-09872-3>, 2022.
- 496 MacKinnon, J., St Laurent, L., and Naveira Garabato, A. C.: Diapycnal mixing processes in the ocean interior, in: *International
497 Geophysics*, vol. 103, Academic Press, 159–183, <https://doi.org/10.1016/B978-0-12-391851-2.00007-6>, 2013.
- 498 Mahadevan, A.: The Impact of Submesoscale Physics on Primary Productivity of Plankton, *Ann. Rev. Mar. Sci.*, 8, 161–184,
499 <https://doi.org/10.1146/annurev-marine-010814-015912>, 2016.
- 500 Mahadevan, A., Pascual, A., Rudnick, D. L., Ruiz, S., Tintoré, J., and D’Asaro, E.: Coherent pathways for vertical transport
501 from the surface ocean to interior, *Bull. Am. Meteorol. Soc.*, 101, E1996–E2004, [https://doi.org/10.1175/BAMS-D-19-
502 0305.1](https://doi.org/10.1175/BAMS-D-19-
502 0305.1), 2020a.



- 503 Mahadevan, A., D'Asaro, E. A., Allen, J. T., Almaraz García, P., Alou-Font, E., Aravind, H. M., Balaguer, P., Caballero, I.,
504 Calafat, N., Carbornero, A., Casas, B., Castilla, C., Centurioni, L. R., Conley, M., Cristofano, G., Cutolo, E., Dever, M.,
505 Enrique Navarro, A., Falcieri, F., Freilich, M., Goodwin, E., Graham, R., Guigand, C., Hodges, B. A., Huntley, H.,
506 Johnston, S., Lankhorst, M., Lermusiaux, P. F. J., Lizaran, I., Mirabito, C., Miralles, A., Mourre, B., Navarro, G., Ohmart,
507 M., Ouala, S., Ozgokmen, T. M., Pascual, A., Pou, J. M. H., Poulain, P. M., Ren, A., Rodriguez Tarry, D., Rudnick, D. L.,
508 Rubio, M., Ruiz, S., Rypina, I. I., Tintore, J., Send, U., Shcherbina, A. Y., Torner, M., Salvador-Vieira, G., Wirth, N., and
509 Zarokanellos, N.: CALYPSO 2019 Cruise Report: field campaign in the Mediterranean, Woods Hole Oceanographic
510 Institution, <https://doi.org/10.1575/1912/25266>, 2020b.
- 511 McDougall, T. J., Thorpe, S. A., and Gibson, C. H.: Small-Scale Turbulence and Mixing in the Ocean: A Glossary, in: Small-
512 scale turbulence and mixing in the ocean, vol. 46, edited by: Nihoul, J. C. J. and Jamart, B. M., Elsevier, 3–9,
513 [https://doi.org/10.1016/S0422-9894\(08\)70533-6](https://doi.org/10.1016/S0422-9894(08)70533-6), 1988.
- 514 McDougall, T. J., Barker, P. M., and Stanley, G. J.: Spice Variables and Their Use in Physical Oceanography, *J. Geophys.*
515 *Res. Ocean.*, 126, e2019JC01593, <https://doi.org/10.1029/2019JC015936>, 2021.
- 516 McWilliams, J. C.: Oceanic Frontogenesis, *Ann. Rev. Mar. Sci.*, 13, 227–253, [https://doi.org/10.1146/annurev-marine-](https://doi.org/10.1146/annurev-marine-032320-120725)
517 [032320-120725](https://doi.org/10.1146/annurev-marine-032320-120725), 2021.
- 518 Mena, C., Reglero, P., Hidalgo, M., Sintes, E., Santiago, R., Martín, M., Moyà, G., and Balbín, R.: Phytoplankton community
519 structure is driven by stratification in the oligotrophic mediterranean sea, *Front. Microbiol.*, 10, 456694,
520 <https://doi.org/10.3389/fmicb.2019.01698>, 2019.
- 521 Mouriño-Carballido, B., Otero Ferrer, J. L., Fernández Castro, B., Marañón, E., Blazquez Maseda, M., Aguiar-González, B.,
522 Chouciño, P., Graña, R., Moreira-Coello, V., and Villamaña, M.: Magnitude of nitrate turbulent diffusion in contrasting
523 marine environments, *Sci. Rep.*, 11, 1–16, <https://doi.org/10.1038/s41598-021-97731-4>, 2021.
- 524 Nasmyth, P. W.: Oceanic turbulence, Ph.D. thesis, University of British Columbia, Canada,
525 <https://doi.org/10.14288/1.0302459>, 1970.
- 526 Oguz, T., Macias, D., Garcia-Lafuente, J., Pascual, A., and Tintore, J.: Fueling plankton production by a meandering frontal
527 jet: A case study for the Alboran sea (Western Mediterranean), *PLoS One*, 9, e111482,
528 <https://doi.org/10.1371/journal.pone.0111482>, 2014.
- 529 Olita, A., Capet, A., Claret, M., Mahadevan, A., Poulain, P. M., Ribotti, A., Ruiz, S., Tintoré, J., Tovar-Sánchez, A., and
530 Pascual, A.: Frontal dynamics boost primary production in the summer stratified Mediterranean sea, *Ocean Dyn.*, 67, 767–
531 782, <https://doi.org/10.1007/s10236-017-1058-z>, 2017.
- 532 Omand, M. M., D'Asaro, E. A., Lee, C. M., Perry, M. J., Briggs, N., Cetinić, I., and Mahadevan, A.: Eddy-driven subduction
533 exports particulate organic carbon from the spring bloom, *Science*, 348, 222–225, <https://doi.org/10.1126/science.1260062>,
534 2015.
- 535 Onken, R. and Brambilla, E.: Double diffusion in the Mediterranean Sea: Observation and parameterization of salt finger
536 convection, *J. Geophys. Res. Ocean.*, 108, 8124, <https://doi.org/10.1029/2002jc001349>, 2003.



- 537 Pinkel, R., Sherman, J., Smith, J., and Anderson, S.: Strain: Observations of the Vertical Gradient of Isopycnal Vertical
538 Displacement, *J. Phys. Oceanogr.*, 21, 527–540, [https://doi.org/10.1175/1520-0485\(1991\)021<0527:sootvg>2.0.co;2](https://doi.org/10.1175/1520-0485(1991)021<0527:sootvg>2.0.co;2),
539 1991.
- 540 Ramondenc, S., Madeleine, G., Lombard, F., Santinelli, C., Stemmann, L., Gorsky, G., and Guidi, L.: An initial carbon export
541 assessment in the Mediterranean Sea based on drifting sediment traps and the Underwater Vision Profiler data sets, *Deep.*
542 *Res. Part I Oceanogr. Res. Pap.*, 117, 107–119, <https://doi.org/10.1016/j.dsr.2016.08.015>, 2016.
- 543 Reale, M., Giorgi, F., Solidoro, C., Di Biagio, V., Di Sante, F., Mariotti, L., Farneti, R., and Sannino, G.: The Regional Earth
544 System Model RegCM-ES: Evaluation of the Mediterranean Climate and Marine Biogeochemistry, *J. Adv. Model. Earth*
545 *Syst.*, 12, e2019MS001812, <https://doi.org/10.1029/2019MS001812>, 2020.
- 546 Rudnick, D. L. and Klinke, J.: The underway conductivity-temperature-depth instrument, *J. Atmos. Ocean. Technol.*, 24,
547 1910–1923, <https://doi.org/10.1175/JTECH2100.1>, 2007.
- 548 Rudnick, D. L., Zarokanellos, N. D., and Tint, J.: A Four-Dimensional Survey of the Almeria–Oran Front by Underwater
549 Gliders: Tracers and Circulation, *J. Phys. Oceanogr.*, 52, 225–242, <https://doi.org/10.1175/JPO-D-21-0181.1>, 2022.
- 550 Ruiz, S., Claret, M., Pascual, A., Olita, A., Troupin, C., Capet, A., Tovar-Sánchez, A., Allen, J., Poulain, P. M., Tintoré, J.,
551 and Mahadevan, A.: Effects of Oceanic Mesoscale and Submesoscale Frontal Processes on the Vertical Transport of
552 Phytoplankton, *J. Geophys. Res. Ocean.*, 124, 5999–6014, <https://doi.org/10.1029/2019JC015034>, 2019.
- 553 Sala, I., Bolado-Penagos, M., Bartual, A., Bruno, M., García, C. M., López-Urrutia, Á., González-García, C., and Echevarría,
554 F.: A Lagrangian approach to the Atlantic Jet entering the Mediterranean Sea: Physical and biogeochemical
555 characterization, *J. Mar. Syst.*, 226, 103652, <https://doi.org/10.1016/j.jmarsys.2021.103652>, 2022.
- 556 Sánchez-Garrido, J. C. and Nadal, I.: The Alboran Sea circulation and its biological response: A review, *Front. Mar. Sci.*, 9,
557 933390, <https://doi.org/10.3389/fmars.2022.933390>, 2022.
- 558 Schmitt, R. W.: Double-Diffusive Convection, in: *Encyclopedia of Ocean Sciences*, Academic Press, 162–170,
559 <https://doi.org/10.1016/B978-012374473-9.00604-4>, 2009.
- 560 Schroeder, K., Chiggiato, J., Bryden, H. L., Borghini, M., and Ben Ismail, S.: Abrupt climate shift in the Western
561 Mediterranean Sea, *Sci. Rep.*, 6, 1–7, <https://doi.org/10.1038/srep23009>, 2016.
- 562 Schulz, K., Mohrholz, V., Fer, I., Janout, M., Hoppmann, M., Schaffer, J., and Koenig, Z.: A full year of turbulence
563 measurements from a drift campaign in the Arctic Ocean 2019–2020, *Sci. Data*, 9, 1–11, <https://doi.org/10.1038/s41597-022-01574-1>, 2022.
- 565 Sheehan, P. M. F., Damerell, G. M., Leadbitter, P. J., Heywood, K. J., and Hall, R. A.: Turbulent kinetic energy dissipation
566 rate and associated fluxes in the western tropical Atlantic estimated from ocean glider observations, *Ocean Sci.*, 19, 77–
567 92, <https://doi.org/10.5194/os-19-77-2023>, 2023.
- 568 Shroyer, E. L., Nash, J. D., Waterhouse, A. F., and Moum, J. N.: Measuring Ocean Turbulence, in: *Observing the Oceans in*
569 *Real Time*, edited by: Venkatesan, R., Tandon, A., D’Asaro, E., and Atmanand, M. A., Springer, Cham, 99–122,
570 https://doi.org/10.1007/978-3-319-66493-4_6, 2018.



- 571 Storer, B. A., Buzzicotti, M., Khatri, H., Griffies, S. M., and Aluie, H.: Global energy spectrum of the general oceanic
572 circulation, *Nat. Commun.*, 13, 1–9, <https://doi.org/10.1038/s41467-022-33031-3>, 2022.
- 573 Stukel, M. R., Aluwihare, L. I., Barbeau, K. A., Chekalyuk, A. M., Goericke, R., Miller, A. J., Ohman, M. D., Ruacho, A.,
574 Song, H., Stephens, B. M., and Landry, M. R.: Mesoscale ocean fronts enhance carbon export due to gravitational sinking
575 and subduction, *Proc. Natl. Acad. Sci. U. S. A.*, 114, 1252–1257, <https://doi.org/10.1073/pnas.1609435114>, 2017.
- 576 Sudre, F., Hernández-Carrasco, I., Mazoyer, C., Sudre, J., Dewitte, B., Garçon, V., and Rossi, V.: An ocean front dataset for
577 the Mediterranean sea and southwest Indian ocean, *Sci. Data*, 10, 1–15, <https://doi.org/10.1038/s41597-023-02615-z>, 2023.
- 578 Tanhua, T., Hainbucher, D., Schroeder, K., Cardin, V., Álvarez, M., and Civitarese, G.: The Mediterranean Sea system: A
579 review and an introduction to the special issue, *Ocean Sci.*, 9, 789–803, <https://doi.org/10.5194/os-9-789-2013>, 2013.
- 580 Taylor, G. I.: Statistical theory of turbulence, *Proc. R. Soc. London. Ser. A - Math. Phys. Sci.*, 151, 421–444,
581 <https://doi.org/10.1098/rspa.1935.0158>, 1935.
- 582 Thomas, L. N., Taylor, J. R., Ferrari, R., and Joyce, T. M.: Symmetric instability in the Gulf Stream, *Deep. Res. Part II Top.*
583 *Stud. Oceanogr.*, 91, 96–110, <https://doi.org/10.1016/j.dsr2.2013.02.025>, 2013.
- 584 Thorpe, S. A.: An introduction to ocean turbulence, Cambridge University Press, England, 291 pp.,
585 <https://doi.org/10.1017/CBO9780511801198>, 2007.
- 586 Thorpe, S. A.: The turbulent ocean, Cambridge University Press, England, 439 pp.,
587 <https://doi.org/10.1017/CBO9780511819933>, 2005.
- 588 van der Boog, C. G., Dijkstra, H. A., Pietrzak, J. D., and Katsman, C. A.: Double-diffusive mixing makes a small contribution
589 to the global ocean circulation, *Commun. Earth Environ.*, 2, 1–9, <https://doi.org/10.1038/s43247-021-00113-x>, 2021.
- 590 van Haren, H.: Sensitive Temperature Probes Detail Different Turbulence Processes in the Deep Mediterranean,
591 *Oceanography*, 36, <https://doi.org/10.5670/OCEANOLOG.2023.108>, 2023.
- 592 van Haren, H., Millot, C., and Taupier-Letage, I.: Fast deep sinking in Mediterranean eddies, *Geophys. Res. Lett.*, 33, 4606,
593 <https://doi.org/10.1029/2005GL025367>, 2006.
- 594 Vladoiu, A., Bouruet-Aubertot, P., Cuyppers, Y., Ferron, B., Schroeder, K., Borghini, M., and Leizour, S.: Contrasted mixing
595 efficiency in energetic versus quiescent regions: Insights from microstructure measurements in the Western Mediterranean
596 Sea, *Prog. Oceanogr.*, 195, 102594, <https://doi.org/10.1016/j.pocean.2021.102594>, 2021.
- 597 Williams, C., Sharples, J., Green, M., Mahaffey, C., and Rippeth, T.: The maintenance of the subsurface chlorophyll maximum
598 in the stratified western Irish Sea, *Limnol. Oceanogr. Fluids Environ.*, 3, 61–73, <https://doi.org/10.1215/21573689-2285100>, 2013.
- 600 Williams, R. G.: Ocean Subduction, in: *Encyclopedia of Ocean Sciences: Second Edition*, Academic Press, 156–166,
601 <https://doi.org/10.1016/B978-012374473-9.00109-0>, 2001.
- 602 Yebra, L., Herrera, I., Mercado, J. M., Cortés, D., Gómez-Jakobsen, F., Alonso, A., Sánchez, A., Salles, S., and Valcárcel-
603 Pérez, N.: Zooplankton production and carbon export flux in the western Alboran Sea gyre (SW Mediterranean), *Prog.*
604 *Oceanogr.*, 167, 64–77, <https://doi.org/10.1016/j.pocean.2018.07.009>, 2018.



- 605 Zarokanellos, N. D., Rudnick, D. L., Garcia-Jove, M., Moure, B., Ruiz, S., Pascual, A., and Tintoré, J.: Frontal Dynamics in
606 the Alboran Sea: 1. Coherent 3D Pathways at the Almeria-Oran Front Using Underwater Glider Observations, *J. Geophys.*
607 *Res. Ocean.*, 127, e2021JC017405, <https://doi.org/10.1029/2021JC017405>, 2022.
- 608 Zhou, H., Dewar, W., Yang, W., Liu, H., Chen, X., Li, R., Liu, C., and Gopalakrishnan, G.: Observations and modeling of
609 symmetric instability in the ocean interior in the Northwestern Equatorial Pacific, *Commun. Earth Environ.*, 3, 1–11,
610 <https://doi.org/10.1038/s43247-022-00362-4>, 2022.
- 611 Zippel, S. F., Farrar, J. T., Zappa, C. J., and Plueddemann, A. J.: Parsing the Kinetic Energy Budget of the Ocean Surface
612 Mixed Layer, <https://doi.org/10.1029/2021GL095920>, 28 January 2022.
- 613